Tumour Marker Prognostic Study

INTERNATIONAL JOURNAL OF SURGERY

OPEN

Noninvasive prediction of perineural invasion in intrahepatic cholangiocarcinoma by clinicoradiological features and computed tomography radiomics based on interpretable machine learning: a multicenter cohort study

Ziwei Liu, MD[a], Chun Luo, MD[b], Xinjie Chen, MD[a], Yanqiu Feng, PhD[a,d,e,f], Jieying Feng, MD[c], Rong Zhang, MD[a], Fusheng Ouyang, MD[a], Xiaohong Li, MD[a], Zhilin Tan, MD[a], Lingda Deng, MD[a], Yifan Chen, MD[a], Zhiping Cai, MD[a], Ximing Zhang, MD[b], Jiehong Liu, MD[d], Wei Liu, MD[a], Baoliang Guo, MD[a,*], Qiugen Hu, MD[a,*]

Background: Perineural invasion (PNI) of intrahepatic cholangiocarcinoma (ICC) is a strong independent risk factor for tumour recurrence and long-term patient survival. However, there is a lack of noninvasive tools for accurately predicting the PNI status. The authors develop and validate a combined model incorporating radiomics signature and clinicoradiological features based on machine learning for predicting PNI in ICC, and used the Shapley Additive explanation (SHAP) to visualize the prediction process for clinical application.

Methods: This retrospective and prospective study included 243 patients with pathologically diagnosed ICC (training, $n=136$; external validation, $n=81$; prospective, $n=26$, respectively) who underwent preoperative contrast-enhanced computed tomography between January 2012 and May 2023 at three institutions (three tertiary referral centres in Guangdong Province, China). The ElasticNet was applied to select radiomics features and construct signature derived from computed tomography images, and univariate and multivariate analyses by logistic regression were used to identify the significant clinical and radiological variables with PNI. A robust combined model incorporating radiomics signature and clinicoradiological features based on machine learning was developed and the SHAP was used to visualize the prediction process. A Kaplan–Meier survival analysis was performed to compare prognostic differences between PNI-positive and PNI-negative groups and was conducted to explore the prognostic information of the combined model.

Results: Among 243 patients (mean age, 61.2 years ± 11.0 (SD); 152 men and 91 women), 108 (44.4%) were diagnosed as PNI-positive. The radiomics signature was constructed by seven radiomics features, with areas under the curves of 0.792, 0.748, and 0.729 in the training, external validation, and prospective cohorts, respectively. Three significant clinicoradiological features were selected and combined with radiomics signature to construct a combined model using machine learning. The eXtreme Gradient Boosting exhibited improved accuracy and robustness (areas under the curves of 0.884, 0.831, and 0.831, respectively). Survival analysis showed the construction combined model could be used to stratify relapse-free survival (hazard ratio, 1.933; 95% CI: 1.093–3.418; $P=0.021$).

Conclusions: We developed and validated a robust combined model incorporating radiomics signature and clinicoradiological features based on machine learning to accurately identify the PNI statuses of ICC, and visualize the prediction process through SHAP for clinical application.

Keywords: Computed tomography, intrahepatic cholangiocarcinoma, perineural invasion, radiomics, the shapley additive explanation

[a]Department of Radiology,Southern Medical University (The First People's Hospital of Shunde), [b]Department of Radiology, The First People's Hospital of Foshan, [c]Department of Radiology, The Sixth Affiliated Hospital, South China University of Technology, Foshan, [d]School of Biomedical Engineering, Southern Medical University, [e]Guangdong Provincial Key Laboratory of Medical Image Processing & Guangdong Province Engineering Laboratory for Medical Imaging and Diagnostic Technology and [f]Guangdong-Hong Kong-Macao Greater Bay Area Centre for Brain Science and Brain-Inspired Intelligence & Key Laboratory of Mental Health of the Ministry of Education, 1023 Sha-Tai South Road, Guangzhou, China

Z.L., C.L., X.C., Y.F. contributed equally to this work.

Z.L., C.L., X.C. and Y.F. referred to the co-first-authors while B.G. and Q.H. referred to the co-corresponding-author.

Sponsorships or competing interests that may be relevant to content are disclosed at the end of this article.

**Corresponding author. Address: Department of Radiology, Shunde Hospital, Southern Medical University (The First People's Hospital of Shunde), No. 1 Jiazi Road, Lunjiao, Shunde District, Foshan, 528308, China. Tel.: +86 139 282 060 09; fax: +86 757 22223899. E-mail: hu6009@163.com (Q. Hu), and Tel.: +86 138 234 073 82; fax: +86 757 22223899. E-mail: tomcatccks@163.com (B. Guo).*

International Journal of Surgery (2024) 110:1039–1051

Received 4 August 2023; Accepted 22 October 2023

Supplemental Digital Content is available for this article. Direct URL citations are provided in the HTML and PDF versions of this article on the journal's website, www.lww.com/international-journal-of-surgery.

Published online 3 November 2023

http://dx.doi.org/10.1097/JS9.0000000000000881

Introduction

Intrahepatic cholangiocarcinoma (ICC) accounts for 10–15% of primary liver cancers, showing a gradual increase in incidence and mortality rate globally[1]. Surgical resection is the primary treatment for patients with ICC. However, the recurrence rate is relatively high, ~57.9–73.4%, which is the main cause of post-operative death[2]. Due to the lack of effective treatment, the overall prognosis of resected patients remains dismal, with a 5-year survival rate of only 20–40%[3].

Perineural invasion (PNI) is characterized by the infiltration of tumour cells along the nerves and/or within the neuronal sheath's epineural, perineural, and endoneurial regions, encompassing at least one-third of the nerves circumference[4]. As a potential route of tumour spread, it has been proposed as a strong independent risk factor for tumour recurrence and long-term survival in ICC[5,6], and the ICC patients with PNI may benefit from a wide resection margin[7,8]. Therefore, preoperative PNI prediction is important for making treatment decisions, helping develop individualized treatment plans, and improving the prognosis of patients with ICC.

Computed tomography (CT) is a common noninvasive imaging method important for ICC diagnosis and preoperative evaluation. However, it is challenging for radiologists to assess the PNI status based on macroscopic CT images. Radiomics converts medical radiologic images into high-throughput quantitative features, thus providing information about tumour pathophysiology. It has shown great potential in characterizing tumour phenotypes and improving cancer diagnosis, prognosis, and treatment response[9]. Traditional machine learning often lacks interpretability, leading to the "black box" problem, which is not conducive to clinical application. The Shapley additive explanation (SHAP), an emerging interpretability method, can explain the "black box" problem from both global and local domains[10,11]. To our knowledge, the noninvasive PNI prediction in ICC using clinicoradiological features and CT radiomics based on interpretable machine learning has not been well established in the literature.

This multicenter study aimed to develop and validate a robust combined model incorporating radiomics signature and clinicoradiological features based on machine learning for predicting PNI in patients with ICC. Additionally, the combined model will utilize SHAP to intuitively interpret the predicted process for clinical application.

HIGHLIGHTS

- In a retrospective and prospective study of 243 patients with intrahepatic cholangiocarcinoma, the radiomics signature based on computed tomography images could identify the Perineural invasion status.
- The combined model incorporating radiomics signature and clinicoradiological features was more accurate and robust, and can be used to stratify relapse-free survival.
- The visualization prediction process through the Shapley Additive explanation is helpful for personalized clinical decision-making.

Materials and methods

Participants

This study included two retrospective cohorts and one prospective cohort from three institutions: Shunde Hospital, Southern Medical University (institution I); the Sixth Affiliated Hospital, South China University of Technology (institution II); and and the First People's Hospital of Foshan (institution III). This study was approved by the institutional review board of Shunde Hospital, Southern Medical University. Written informed consent was obtained from each prospectively enroled participant. For retrospective cohorts, the requirement of informed consent was waived. This study had been reported in line with the REMARK criteria[12].

Between January 2012 and May 2023, preoperative contrast-enhanced CT images and clinical data from 497 patients with pathologically confirmed ICC were collected from three institutions in China. Of these, 243 were included in the final analysis. Ninety-four and 42 patients from institutions I and II were recruited as a total of 136 patients in the training cohort. Eighty-one patients were recruited as an external validation cohort from institution III. Twenty-six patients were recruited as a prospective cohort from institution III. Data were censored on 2 June 2023. The inclusion criteria were: (a) patients with pathologically confirmed ICC and (b) patients who underwent preoperative contrast-enhanced CT. The exclusion criteria were: (a) patients who did not receive curative resection, (b) incomplete clinical or pathological data, (c) received previous treatment, (d) poor image quality with obvious artifacts, and (e) CT examination performed more than 1 month before surgery. The inclusion and exclusion processes are illustrated in Fig. 1.

Clinical data collection and follow-up

The following clinical data of each patient were recorded from the medical record archives of participating institutions: age, sex, chronic hepatitis, cirrhosis, clonorchis sinensis infestation, alpha-fetoprotein (AFP, ug/l), carcinoembryonic antigen (CEA, ug/l), cancer antigen 12-5 (CA12-5, U/ml), carbohydrate antigen 19-9 (CA19-9, U/ml), alanine aminotransferase (ALT, U/l), aspartate aminotransferase (AST, U/l), gamma-glutamyl transferase (GGT, U/l), neutrophil-to-lymphocyte ratio (NLR), platelet to lymphocyte ratio (PLR), and Child-Pugh classification. Preoperative TMN stage was evaluated by CT, MRI, and/or whole-body PET/CT, basing on the 8th edition of the American Joint Committee on Cancer (AJCC) staging system.

Considering sufficient follow-up time, the patients in institution III were followed up every 3–6 months after surgery by enhanced ultrasound, CT or MRI until recurrence or the end of 31 December 2022. Relapse-free survival (RFS) was defined as the time from surgery date to the date of first recurrence, metastasis or last follow-up.

Histopathological examination

The histologic sections from three institutions were evaluated using the same criteria by two experienced pathologists from institution I without knowledge of the patients' clinical data. They made comprehensive judgments based on gross specimens or radiographic images, combined with microscopic histopathological examination[13]. A third senior pathologist was consulted in

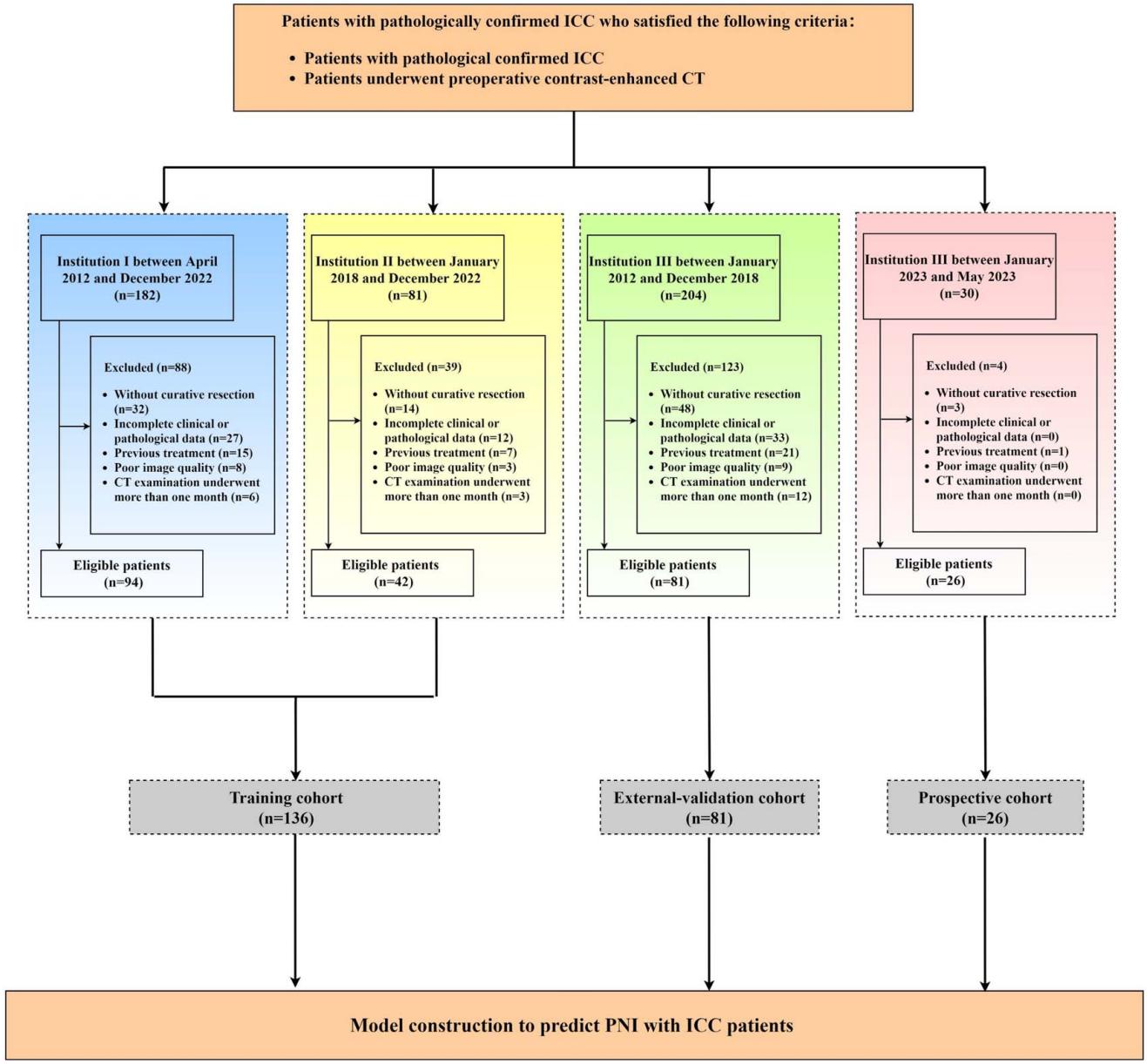

Figure 1. Flowchart of inclusion and exclusion criteria for eligible patients in the study. CT, computed tomography; ICC, intrahepatic cholangiocarcinoma; PNI, perineural invasion.

the event of inconsistencies. According to the definition[4], PNI was divided into positive (+) and negative (−) groups.

CT technique

The CT scanners and scanning parameters for each institution are shown in Supplement Table 1, Supplemental Digital Content 1, http://links.lww.com/JS9/B281. For each patient, a triple-phase CT scan was performed, including a plain scan and arterial and portal venous phases. Using bolus tracking technique, arterial and portal venous phase images were acquired at 30 and 60 s, respectively. The contrast agents (Ioversol 320 iodine/ml, Jiangsu Hengrui Medicine Corp. Ltd.; or Omnipaque 300 mg iodine/ml, GE Healthcare) were injected at a speed of 3.0–4.0 ml/s with a high-pressure pump syringe.

Semantic features of computed tomography

Two radiologists with eight (Reader 1) and 15 (Reader 2) years of experience in abdominal diagnosis were selected to independently assess CT image features; they were aware that the lesions were ICC but were blinded to all other clinical and histopathologic information. Discrepancies were resolved by consensus after reevaluating the images. Inter-reader variation of semantic features was measured with κ-statistic ($\kappa > 0.75$ was considered excellent agreement; $0.40 \leq \kappa \leq 0.75$, good; $\kappa < 0.40$, poor). In patients with multiple tumours, the largest tumour size was

analyzed. The following CT image features were evaluated: (a) tumour size; (b) tumour morphology; (c) tumour number; (d) tumour location; (e) tumour capsule; (f) intrahepatic bile duct dilatation; (g) intrahepatic bile duct calculus; (h) satellite nodules; (i) surface retraction; (j) peritumoral arterial hyperenhancement; (k) arterial phase enhancement; (l) dynamic enhancement pattern. The evaluation of CT image features is shown in Supplement Figure 1, Supplemental Digital Content 1, http://links.lww.com/JS9/B281, and a more detailed description in Supplement Method.

Image pre-processing and tumour segmentation

All original CT images were appropriately pre-processed to minimize the centre effect from different institutions and scanners[14]. To standardize the voxel spacing, images were isotropically resampled to a voxel dimension of $1\times1\times1$ mm^3 (x, y, z). To reduce noise and discretize intensities, the Hounsfield units were set to 25 bins[15–17]. A radiologist with five years of abdominal diagnosis experience (Reader 3) segmented the tumour using three-dimensional Slicer (version 4.10.2; http://www.slicer.org). The tumour volume of interest (VOI_{tumour}) was manually drawn on each transverse section from the arterial and portal venous phases. In reference to previous peritumoral radiomics studies[18,19], the peritumoral VOI ($VOI_{10\ mm}$) was defined as 10 mm. The entire VOI ($VOI_{tumour+10\ mm}$) included the tumour and the peritumoral VOIs. The segmentation results were validated by a senior radiologist with ten years of abdominal diagnosis experience (Reader 4) who randomly selected 30 samples from a cohort. The reproducibility of the extracted features was evaluated by the inter-class correlation coefficient. Finally, the VOI_{tumour}, $VOI_{10\ mm}$, and $VOI_{tumour+10\ mm}$ were saved for subsequent quantitative feature extraction.

Radiomics feature extraction, standardization, and selection

Feature extraction was performed using the open-source pyradiomics package in the three-dimensional Slicer extension manager, which included shape, first-order, and texture features[16]. All radiomics features were standardized using z-scores and ComBaTool, a free online application (https://forlhac.shinyapps.io/Shiny_ComBat/)[20,21]. Principal component analysis was used to visualize the correction of batch effects on these features by ComBats. We followed a four-step procedure to identify robust radiomics features in the training cohort. First, features with high stability (inter-class correlation coefficient >0.75) in the test-retest settings were retained for further analysis. Second, univariate statistical analysis was performed on the features, with a significance of $P<0.05$. Third, we used Pearson's or Spearman's correlation analyses ($|r|>0.80$) to ensure low collinearity. Finally, to prevent overfitting of the model, ElasticNet was used to select the final radiomics risk factors of the PNI[22]. The penalty parameter tuning was conducted by 10-fold cross-validation, and the mixing parameters were set to ($\lambda=-1.80$, $\alpha=0.5$). The radscore was determined by weighting the feature coefficients of the model using logistic regression. The radiomics analysis process is illustrated in Fig. 2.

Clinical and radiological risk factors

In the training cohort, individual factors were analyzed for significant differences using the Student's *t*-test or Mann–Whitney U test and the χ^2 test or Fisher's exact test, as appropriate. Univariate and multivariate analyses were used to identify the significant clinical and radiological factors with PNI, which were selected by stepwise logistic regression based on the Akaike information criterion.

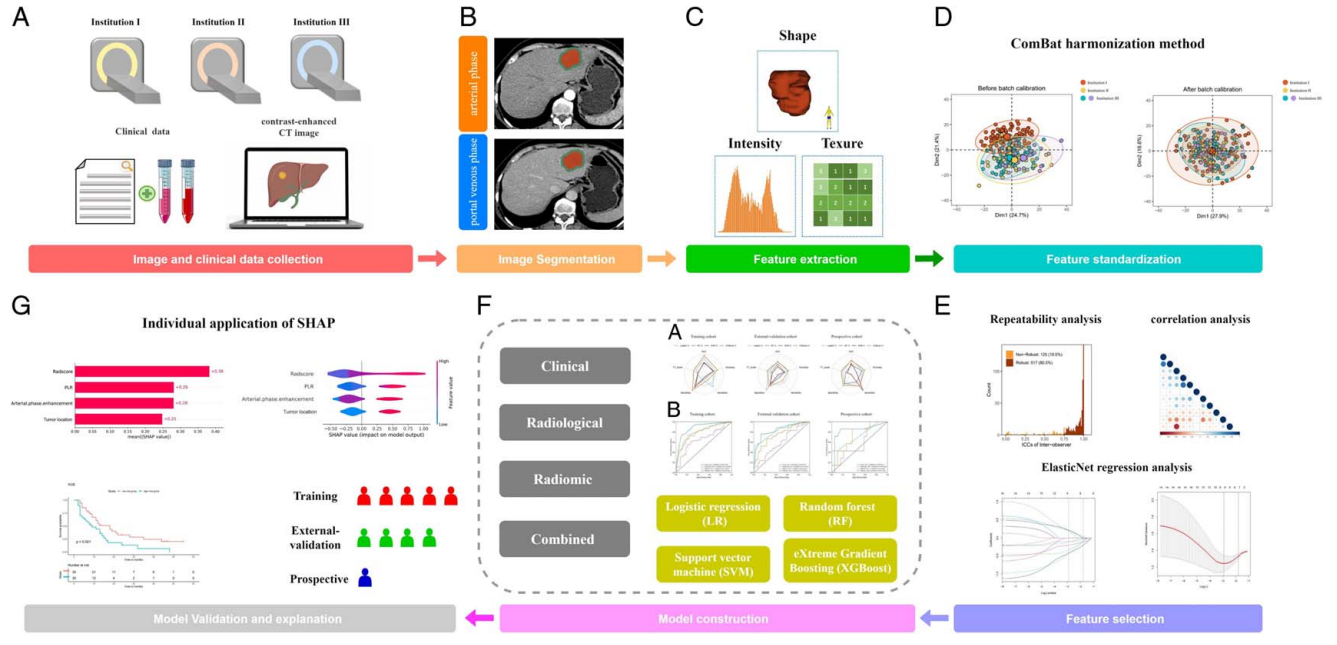

Figure 2. Overall radiomics analysis process in this study. (A) Collection of clinical data and CT images. (B) Tumour segmentation on the arterial and portal venous phases. (C) Radiomics features extraction from dual-phase CT images. (D) All radiomics features were standardized using z-scores and ComBaTool. (E) Radiomic features selection from training cohort using ElasticNet. (F) Construction of the optimization model by comparing different models. (G) Model visualization, validation, and survival prognosis analysis. CT, computed tomography.

Model development and validation

We examined clinical, radiological, radiomics, and combined PNI prediction models to demonstrate the clinical value of the radiomics model. A combined model was built by incorporating radscore and clinicoradiological risk features.

To select the optimal prediction model, four machine-learning algorithms were used to build combined models: logistic regression (LR), eXtreme Gradient Boosting (XGBoost), random forest (RF), and support vector machine (SVM). Each model's performance was evaluated using the receiver operating characteristic (ROC) curve and area under the curve (AUC) values, accuracy, F1 score, sensitivity, and specificity. The DeLong's test was used to compare the AUC differences. Furthermore, the incremental difference between the combined and single models was compared using the net reclassification index (NRI), and the net benefit was determined using decision curve analysis (DCA). Based on the study results, we used SHAP to visualize and analyze the prediction process of the PNI model. Finally, to verify the predictive model's generalizability, external validation, and prospective cohorts were used to validate the prediction performance.

Statistical analysis

Statistical analyses were performed using Python (version 3.7.3; https://www.python.org/) and R software (version 4.0.4; https://www.r-project.org/). The quantitative statistics conforming to the normal distribution were presented as mean ± (SD), and those not conforming to the normal distribution were presented as median [interquartile range]. Qualitative data are expressed as numbers and percentages (*N*, %). Survival curves were drawn using the Kaplan–Meier method and compared using the log-rank test. Odds ratio (OR) was used for logistic regression, and hazard ratio (HR) was used for Cox regression, and 95% CI were set for evaluation and analysis. Statistical significance was set at P less than 0.05.

Results

Baseline characteristics of the study cohorts

Among 243 patients (mean age, 61.2 years ± 11.0 (SD); 152 men and 91 women), 108 (44.4%) were diagnosed with PNI (+). Among these, 38.3% (36/94), 54.8% (23/42), and 45.8% (49/107) were in institutions I, II, and III, respectively. We combined institutions I and II into a training cohort, with PNI incidence rates of 43.4% (59/136). Furthermore, institution III conducted external validation and prospective cohorts chronologically, with PNI prevalence rates of 51.9% (42/81) and 26.9% (7/26), respectively. The clinical data and CT imaging features of the different cohorts are presented in Table 1. The two radiologists (Readers 1 and 2) showed a consistent analysis of qualitative CT features, as the kappa values were all greater than 0.600 (0.650–1.000, $P < 0.001$, Supplement Table 2, Supplemental Digital Content 1, http://links.lww.com/JS9/B281).

Clinicoradiological features associated with PNI

Univariate analysis showed sex, chronic hepatitis, cirrhosis, GGT, PLR, tumour morphology, tumour location, tumour capsule, intrahepatic bile duct dilatation, intrahepatic bile duct calculus, peritumoral arterial hyperenhancement, arterial phase enhancement, and dynamic enhancement pattern were significantly related to the PNI (all $P < 0.05$, Supplement Table 3, Supplemental Digital Content 1, http://links.lww.com/JS9/B281). Multivariate analysis showed that PLR (OR 1.007; 95% CI 1.001–1.013; $P = 0.018$), tumour location (OR 4.351; 95% CI 1.759–10.763; $P = 0.001$), and arterial phase enhancement (OR 6.570; 95% CI 1.744–24.753; $P = 0.005$) were independent predictors of PNI (Supplement Table 4, Supplemental Digital Content 1, http://links.lww.com/JS9/B281).

Radiomics feature extraction, standardisation, and selection

For feature extraction, 107 radiomics features (14 shape features, 18 first-order features, and 75 texture features) were extracted from each three-dimensional segmentation, yielding 642 features for every lesion (VOI_{tumour}, $VOI_{10\ mm}$, and $VOI_{tumour+10\ mm}$ in the arterial and portal venous phases). Supplement Figure 2, Supplemental Digital Content 1, http://links.lww.com/JS9/B281 shows that ComBat normalization aggregated the data distributions of the three institutions, which were scattered before eliminating the centre effects. For feature selection, first, based on the test-retest settings, 125 features were removed, and 517 features were retained. Second, 76 features were roughly selected using an independent-samples *t*-test or Mann–Whitney U test, and 14 low-correlation features were retained using Pearson or Spearman correlation analysis. Finally, the ElasticNet regression analysis determined seven predictive radiomics features (six peritumoral features and one entire feature). Details of the radiomics features selection is illustrated in Supplement Table 5, Supplemental Digital Content 1, http://links.lww.com/JS9/B281 and supplement Figure 3, and the radscore formula is as follows:

$$\begin{aligned}\text{Radscore} = &-1.80 + (0.04117 \times \text{A\_VOI}_{\text{tumor+10mm}}\text{\_glcm\_Correlation})\\ &- (0.00698 \times \text{A\_VOI}_{\text{10mm}}\text{\_10Percentile})\\ &- (0.04098 \times \text{A\_VOI}_{\text{10mm}}\text{\_Median})\\ &- (0.08565 \times \text{A\_VOI}_{\text{10mm}}\text{\_glszm\_GrayLevelNonUniformity})\\ &- (0.10042 \times \text{P\_VOI}_{\text{10mm}}\text{\_90Percentile})\\ &- (0.11367 \times \text{P\_VOI}_{\text{10mm}}\text{\_glcm\_Imc1})\\ &- (0.20315 \times \text{P\_VOI}_{\text{10mm}}\text{\_glcm\_MaximumProbability}).\end{aligned}$$

Prediction models development and validation

The AUC, accuracy, F1 score, sensitivity, and specificity of each model are presented in Table 2. The performance of the radiomics model (AUCs of 0.792, 0.748, and 0.729 in the training external validation, and prospective cohorts, respectively) was superior to that of the clinical model (AUCs of 0.660, 0.601, and 0.586, respectively; DeLong's test, all $P < 0.05$) but comparable to that of the radiological model (AUCs of 0.796, 0.826, and 0.726, respectively; DeLong's test, $P = 0.196$–0.981). The combined model included four commonly used machine-learning models (LR, XGBoost, RF, and SVM), with AUCs exceeding 0.796, 0.755 and 0.714 in training, external validation, and prospective cohorts, respectively. In the training cohort, the XGBoost model outperformed the RF and SVM models (DeLong's test, all $P < 0.05$), but showed no significant difference compared to the LR model (DeLong's test, $P = 0.083$). In the external validation cohort and prospective cohort, there were no significant differences observed between the XGBoost model and the other three machine-learning models (DeLong's test, $P = 0.059$-0.740). However, XGBoost

Table 1

Clinical and CT image characteristics of 243 patients with ICC in different cohorts.

	Training ($n=136$)		External validation ($n=81$)		Prospective ($n=26$)	
Characteristic	**PNI (–) ($n=77$)**	**PNI (+) ($n=59$)**	**PNI (–) ($n=39$)**	**PNI (+) ($n=42$)**	**PNI (–) ($n=19$)**	**PNI (+) ($n=7$)**
Age, mean (SD), year	61.78 (10.08)	60.29 (11.68)	63.77 (9.76)	63.07 (10.67)	55.26 (12.73)	51.71 (9.93)
Sex, *n* (%)						
Female	24 (31.2)	29 (49.2)	17 (43.6)	15 (35.7)	5 (26.3)	1 (14.3)
Male	53 (68.8)	30 (50.8)	22 (56.4)	27 (64.3)	14 (73.7)	6 (85.7)
Chronic hepatitis, *n* (%)						
Absent	48 (62.3)	54 (91.5)	14 (35.9)	10 (23.8)	7 (36.8)	3 (42.9)
Present	29 (37.7)	5 (8.5)	25 (64.1)	32 (76.2)	12 (63.2)	4 (57.1)
Cirrhosis, *n* (%)						
Absent	60 (77.9)	54 (91.5)	32 (82.1)	35 (83.3)	15 (78.9)	7 (100.0)
Present	17 (22.1)	5 (8.5)	7 (17.9)	7 (16.7)	4 (21.1)	0 (0.0)
Clonorchis sinensis infestation, *n* (%)						
Absent	64 (83.1)	53 (89.8)	25 (64.1)	29 (69.0)	15 (78.9)	6 (85.7)
Present	13 (16.9)	6 (10.2)	14 (35.9)	13 (31.0)	4 (21.1)	1 (14.3)
AFP, median [IQR], ug/l	2.63 [1.64, 5.11]	2.87 [1.88, 4.60]	3.07 [2.12, 5.26]	2.83 [2.06, 5.64]	2.14 [1.69, 3.90]	3.27 [2.13, 5.97]
CEA, median [IQR], ug/l	3.38 [1.67, 8.72]	3.44 [2.42, 7.16]	3.43 [2.22, 6.70]	3.51 [1.89, 7.14]	2.64 [1.73, 5.28]	6.85 [3.16, 7.85]
CA12-5, median [IQR], U/ml	19.90 [11.60, 75.35]	40.90 [14.60, 144.19]	16.90 [12.43, 82.53]	17.52 [5.68, 50.61]	44.19 [24.57, 114.54]	48.22 [36.94, 700.26]
CA19-9, median [IQR], U/ml	61.80 [19.80, 465.15]	220.26 [55.30, 2583.03]	59.94 [15.23, 769.30]	36.40 [13.23, 729.98]	113.09 [42.71, 604.32]	719.24 [375.35, 824.90]
ALT, median [IQR], U/l	34.00 [18.50, 58.50]	30.00 [16.00, 122.00]	23.00 [15.50, 41.50]	34.00 [16.25, 101.00]	21.00 [13.50, 41.00]	24.00 [22.50, 37.50]
AST, median [IQR], U/l	30.00 [23.45, 51.00]	36.00 [22.00, 68.00]	23.00 [19.00, 32.00]	32.00 [20.50, 72.75]	27.00 [19.00, 37.00]	34.00 [26.50, 51.50]
GGT, median [IQR], U/l	68.00 [39.25, 149.00]	105.50 [44.00, 251.00]	59.00 [30.00, 156.50]	73.00 [37.00, 226.00]	58.00 [24.50, 150.50]	129.00 [110.50, 455.00]
NLR, median [IQR]	2.94 [2.05, 5.25]	3.18 [2.27, 5.54]	2.47 [1.96, 3.40]	3.01 [2.02, 5.38]	3.21 [2.05, 5.89]	3.24 [2.96, 5.840]
PLR, median [IQR]	134.26 [97.21, 169.28]	184.27 [113.39, 231.82]	131.46 [104.85, 163.22]	144.23 [121.62, 190.86]	159.29 [102.32, 186.65]	150.23 [125.98, 206.67]
Child-Pugh, *n* (%)						
A	76 (98.7)	55 (93.2)	38 (97.4)	37 (88.1)	14 (73.7)	5 (71.4)
B	1 (1.3)	4 (6.8)	1 (2.6)	5 (11.9)	5 (26.3)	2 (28.6)
T stage, *n* (%)						
I–II	39 (50.6)	29 (49.2)	32 (82.1)	26 (61.9)	13 (68.4)	3 (42.9)
III–IV	38 (49.4)	30 (50.8)	7 (17.9)	16 (38.1)	6 (31.6)	4 (57.1)
TNM stage, *n* (%)						
I–II	34 (44.2)	18 (30.5)	27 (69.2)	20 (47.6)	7 (36.8)	2 (28.6)
III–IV	43 (55.8)	41 (69.5)	12 (30.8)	22 (52.4)	12 (63.2)	5 (71.4)
Tumour size, median [IQR], cm	4.80 [2.95, 6.85]	4.90 [3.30, 6.50]	4.90 [3.40, 6.40]	4.20 [3.02, 5.35]	6.30 [5.30, 7.90]	9.30 [7.70, 9.40]
Tumour morphology, *n* (%)						
Mass forming	57 (74.0)	30 (50.8)	38 (97.4)	35 (83.3)	19 (100.0)	7 (100.0)
Non-mass forming	20 (26.0)	29 (49.2)	1 (2.6)	7 (16.7)	0 (0.0)	0 (0.0)
Tumour number, *n* (%)						
Solitary	69 (89.6)	47 (79.7)	34 (87.2)	39 (92.9)	16 (84.2)	4 (57.1)
Multiple	8 (10.4)	12 (20.3)	5 (12.8)	3 (7.1)	3 (15.8)	3 (42.9)
Tumour location, *n* (%)						
Subcapsular	66 (85.7)	25 (42.4)	32 (82.1)	13 (31.0)	16 (84.2)	3 (42.9)
Perihilar	11 (14.3)	34 (57.6)	7 (17.9)	29 (69.0)	3 (15.8)	4 (57.1)
Tumour capsule, *n* (%)						
Complete	33 (42.9)	7 (11.9)	13 (33.3)	9 (21.4)	5 (26.3)	1 (14.3)

Incomplete/none	44 (57.1)	52 (88.1)	26 (66.7)	33 (78.6)	14 (73.7)	6 (85.7)
Intrahepatic bile duct dilatation, *n* (%)						
Absent	35 (45.5)	6 (10.2)	16 (41.0)	6 (14.3)	12 (63.2)	3 (42.9)
Present	42 (54.5)	53 (89.8)	23 (59.0)	36 (85.7)	7 (36.8)	4 (57.1)
Intrahepatic bile duct calculus, *n* (%)						
Absent	66 (85.7)	32 (54.2)	35 (89.7)	25 (59.5)	19 (100.0)	7 (100.0)
Present	11 (14.3)	27 (45.8)	4 (10.3)	17 (40.5)	0	0
Satellite nodules, *n* (%)						
Absent	50 (64.9)	41 (69.5)	25 (64.1)	36 (85.7)	10 (52.6)	2 (28.6)
Present	27 (35.1)	18 (30.5)	14 (35.9)	6 (14.3)	9 (47.4)	5 (71.4)
Surface retraction, *n* (%)						
Absent	55 (71.4)	37 (62.7)	29 (74.4)	32 (76.2)	13 (68.4)	7 (100.0)
Present	22 (28.6)	22 (37.3)	10 (25.6)	10 (23.8)	6 (31.6)	0
Peritumoral arterial hyperenhancement, *n* (%)						
Absent	54 (70.1)	24 (40.7)	19 (48.7)	20 (47.6)	10 (52.6)	3 (42.9)
Present	23 (29.9)	35 (59.3)	20 (51.3)	22 (52.4)	9 (47.4)	4 (57.1)
Arterial phase enhancement, *n* (%)						
Diffuse hyperenhancement	20 (26.0)	5 (8.5)	10 (25.6)	5 (11.9)	4 (21.1)	0
Peripheral rim	48 (62.3)	23 (39.0)	19 (48.7)	7 (16.7)	12 (63.2)	3 (42.9)
Diffuse hypoenhancement	9 (11.7)	31 (52.5)	10 (25.6)	30 (71.4)	3 (15.8)	4 (57.1)
Dynamic enhancement pattern, *n* (%)						
Wash-in and wash-out	16 (20.8)	1 (1.7)	9 (23.1)	4 (9.5)	4 (21.1)	0
Progressive interstitial	53 (68.8)	47 (79.7)	27 (69.2)	28 (66.7)	12 (63.2)	5 (71.4)
Persistent hyperenhancement	5 (6.5)	4 (6.8)	2 (5.1)	3 (7.1)	2 (10.5)	0
Persistent hypoenhancement	3 (3.9)	7 (11.8)	1 (2.6)	7 (16.7)	1 (5.3)	2 (28.6)

AFP, alpha-fetoprotein; ALT, alanine aminotransferase; AST, aspartate aminotransferase; CA12-5, cancer antigen 12-5; CA19-9, carbohydrate antigen 19-9; CEA, carcinoembryonic antigen; CT, computed tomography; GGT, gamma-glutamyl transferase; ICC, intrahepatic cholangiocarcinoma; IQR, interquartile range; NLR, neutrophil-to-lymphocyte ratio; PLR, platelet to lymphocyte ratio.

Table 2

Prediction performance of different models.

Cohort	Model	AUC (95% CI)	Accuracy	F1 score	Sensitivity	Specificity
Training	Clinical	0.660 (0.562–0.750)	0.684	0.626	0.610	0.740
	Radiological	0.796 (0.721–0.868)	0.765	0.729	0.729	0.792
	Radiomic	0.792 (0.717–0.857)	0.750	0.696	0.661	0.818
	LR-C	0.855 (0.788–0.911)	0.779	0.769	0.847	0.727
	XGBoost-C	0.884 (0.824–0.935)	0.831	0.793	0.746	0.896
	RF-C	0.804 (0.734–0.874)	0.779	0.737	0.712	0.831
	SVM-C	0.796 (0.718–0.870)	0.787	0.739	0.695	0.857
External validation	Clinical	0.601 (0.469–0.720)	0.605	0.673	0.786	0.410
	Radiological	0.826 (0.733–0.907)	0.741	0.677	0.524	0.974
	Radiomic	0.748 (0.635–0.843)	0.716	0.709	0.667	0.769
	LR-C	0.839 (0.742–0.920)	0.802	0.778	0.667	0.949
	XGBoost-C	0.831 (0.735–0.915)	0.815	0.810	0.762	0.872
	RF-C	0.794 (0.693–0.885)	0.753	0.744	0.690	0.821
	SVM-C	0.755 (0.645–0.848)	0.741	0.643	0.846	0.72
Prospective	Clinical	0.586 (0.345–0.817)	0.500	0.519	1.000	0.316
	Radiological	0.726 (0.479–0.966)	0.846	0.600	0.429	1.000
	Radiomic	0.729 (0.477–0.925)	0.692	0.600	0.857	0.632
	LR-C	0.850 (0.639–1.000)	0.808	0.706	0.857	0.789
	XGBoost-C	0.831 (0.567–1.000)	0.846	0.750	0.857	0.842
	RF-C	0.714 (0.495–0.938)	0.769	0.625	0.714	0.789
	SVM-C	0.759 (0.534–0.943)	0.615	0.583	1.000	0.474

-C, -combined; AUC, area under the curve; LR, logistic regression; RF, random forest; SVM, support vector machine; XGBoost, eXtreme Gradient Boosting.

exhibited improved accuracy and robustness in all cohorts based on comprehensive predictive metrics. Therefore, we selected the XGBoost model as the optimal combined model (AUCs of 0.884, 0.831, and 0.831, respectively), (Figure 3).

To better illustrate the potential clinical value of the combined model, the incremental differences between the XGBoost combined model and the single model were compared using the NRI, and the net benefit was determined using DCA. Although there

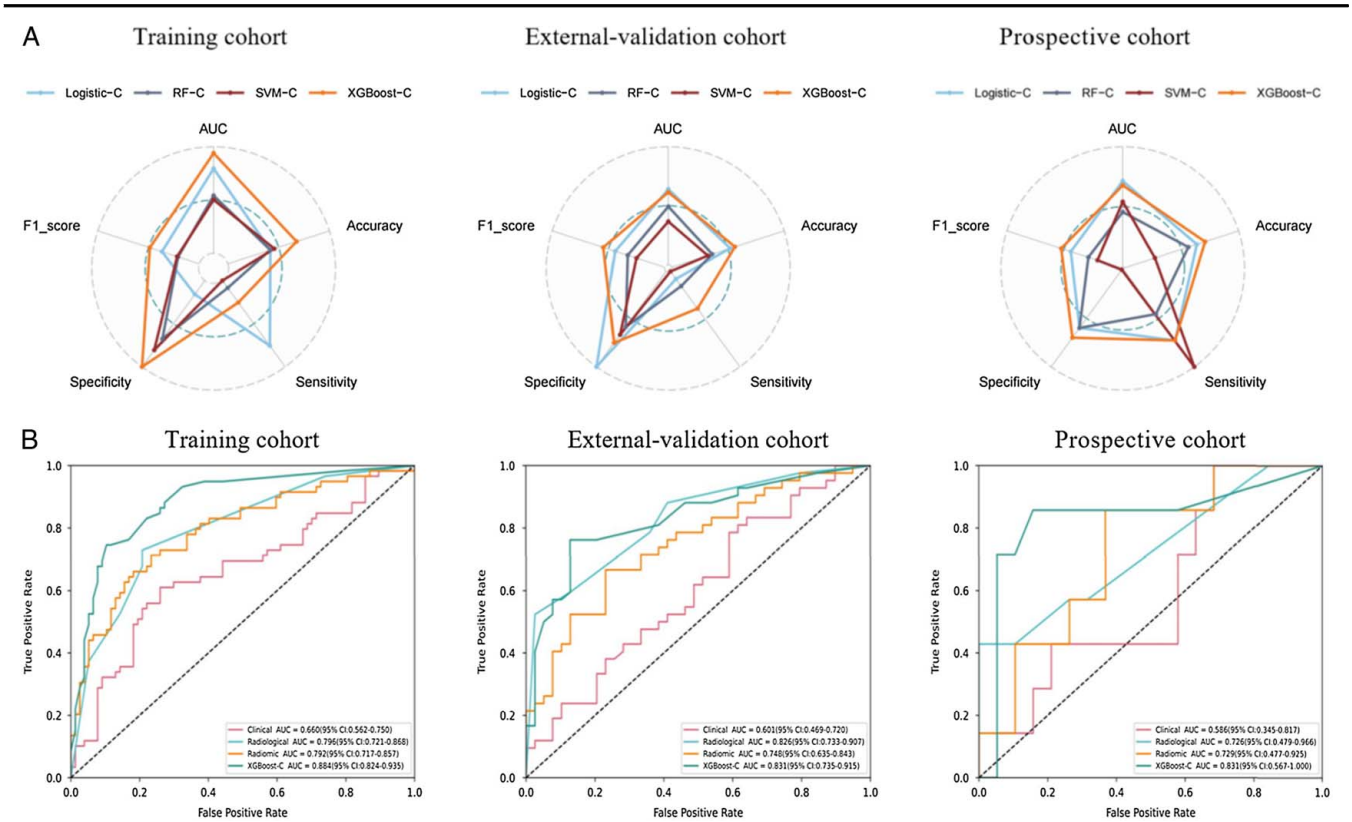

Figure 3. (A) The radar chart visualization of prediction performance for different machine learning combined models. (B) Receiver operating characteristic (ROC) curves. Area under the curve (AUC) and 95% CIs of the training, external, and prospective validation cohorts for the XGBoost combined and single models.

was no statistical difference in AUCs between the XGBoost combined model and the single model in some cohorts, NIRs were greater than 0 in the vast majority of cohorts, indicating that the XGBoost combined model had an improvement, suggesting that its predictive ability was better (Supplement Table 6, Supplemental Digital Content 1, http://links.lww.com/JS9/B281). DCA graphically demonstrated that the XGBoost combined model provided a larger net benefit across the range of reasonable threshold probabilities compared to the single model in all cohorts (Supplement Figure 4, Supplemental Digital Content 1, http://links.lww.com/JS9/B281).

XGBoost combined model for SHAP

We calculated the overall and individual Shapley values for the XGBoost combined model interpretation and clinical application. In the overall visualization, the SHAP bar chart (Fig. 4A) shows the weights of the four most important characteristics (radsocre, PLR, arterial phase enhancement, and tumour location) of the model. The average Shapley values were 0.38, 0.28, 0.28, and 0.25, respectively, with the radscore having the highest weight. The SHAP bees-warm plot (Fig. 4B) shows each feature's positive or negative effects on the prediction probability in red and blue. In predicting the probability of positive PNI expression, the radscore, tumour location, and PLR had a positive effect, while arterial phase enhancement had a negative effect. The SHAP heatmap plot (Fig. 4C) shows each feature's direction and intensity of influence in all model cases, whereas the SHAP decision plot (Fig. 4D) shows the impact process of each significant feature on the final predicted probability. In the individual visualization, Fig. 5 shows four typical examples of correctly predicted PNI positivity and negativity. The SHAP effort plot shows each feature's positive and negative effects on predictive outcomes in a single case. The base value represents the basic prediction probability of the model, and f (x) represents its final prediction probability.

Prognostic analysis of the models

In institution III, 65 patients were successfully followed up. The overall RFS rate was 75.4% (49/65 patients). The median RFS rate of PNI (+) and PNI (–) was 8.0 (range: 2–45 months) and 12.5 months (range: 2–55 months), respectively. Statistically significant differences in RFS between PNI (+) and PNI (–) patients were observed (HR, 1.925; 95% CI: 1.070–3.460; $P = 0.025$) (Fig. 6A). To evaluate the prognostic stratification value of the combined model, patients were divided into predicted PNI (–) (XGBoost <0.413) and PNI (+) (XGBoost >0.413) groups based on the combined model cut-off value by maximizing their Youden index values. Kaplan–Meier survival analyses (Fig. 6B) showed that the combined model could successfully stratify RFS (HR, 1.933; 95% CI: 1.093–3.418; $P = 0.021$).

Discussion

In this study, we established a PNI radiomics signature based on 136 arterial phase- and portal venous phase-enhanced CT images, combined clinical and radiological features to construct a comprehensive model, and compared four commonly used machine-learning models to determine the optimal performance model for predicting PNI in patients with ICC. Its performance was successfully verified in external (81 patients), and prospective cohorts (26 patients). Meanwhile, we compared RFS between PNI from institution III and attempted to evaluate the predictive value of the combined model for RFS. Finally, we used SHAP to visualize the entire model prediction process, from the overall to the individual levels. These results indicate that the combined model incorporating radiomics signature and clinicoradiological features

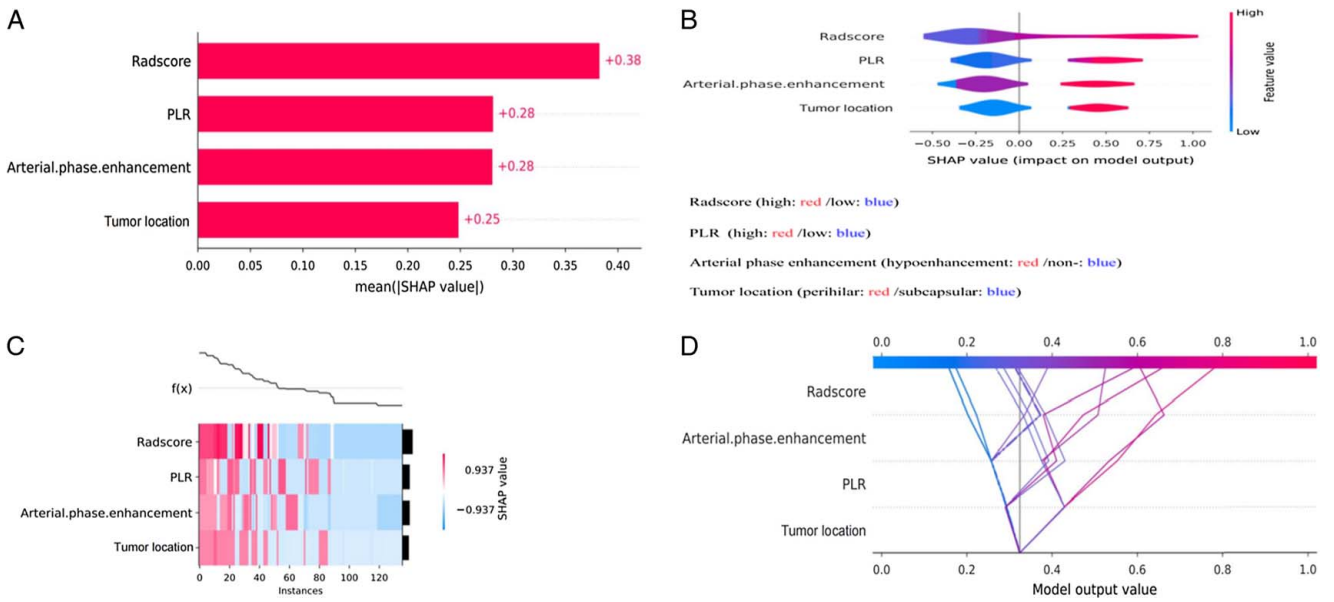

Figure 4. Overall visualization of the model through SHAP. (A) The SHAP bar chart shows the weight of the four most important characteristics in the model. (B) The SHAP bees-warm plot shows the positive or negative effects of each feature on the prediction probability through red and blue colours. (C) The SHAP heatmap plot shows the direction and intensity of influence for each feature of all cases in the model. (D) The SHAP decision plot shows the impact process of each significant features on the final predicted probability. PLR, platelet to lymphocyte ratio; SHAP, Shapley Additive explanation.

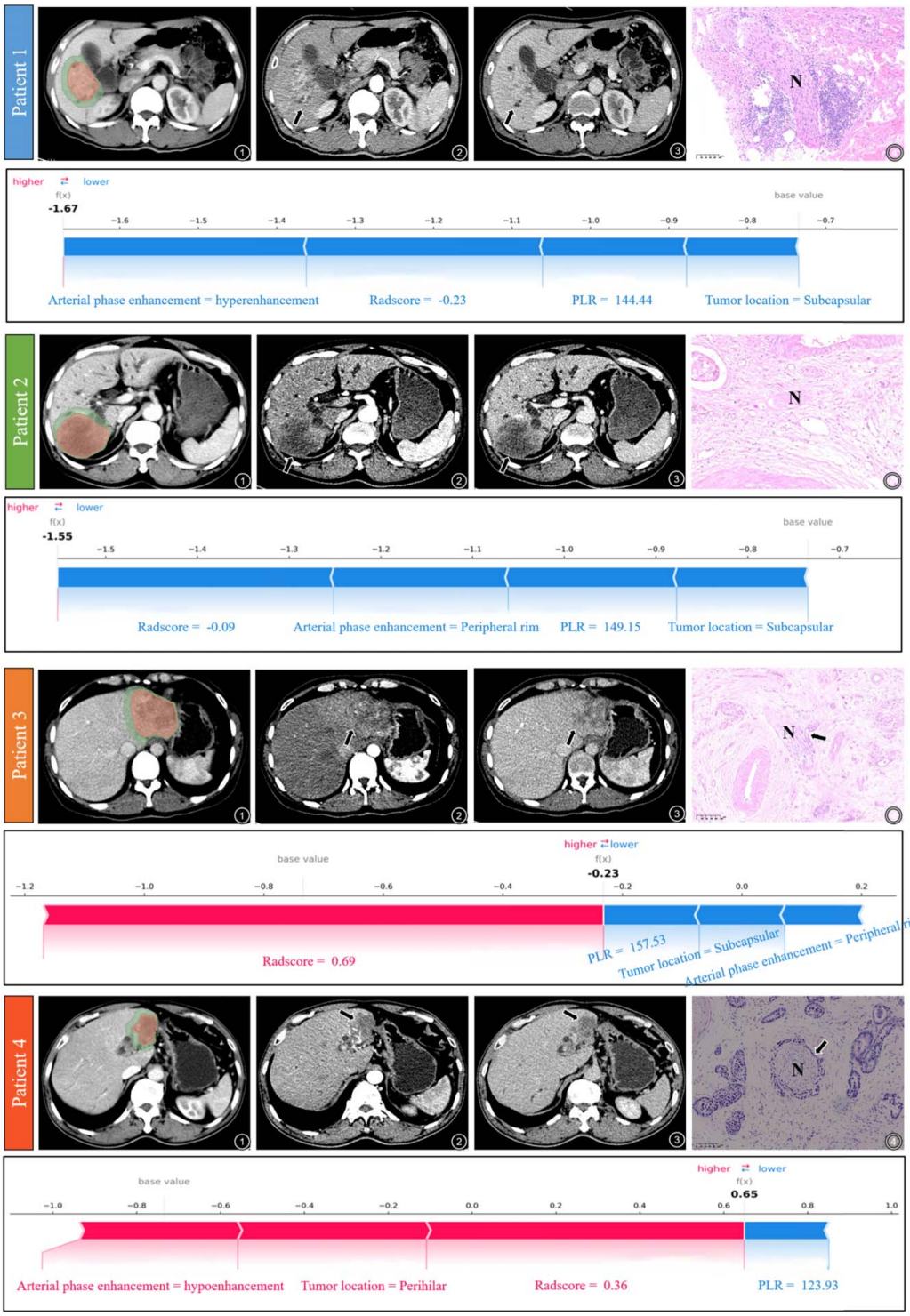

Figure 5. Individual visualization of the mode through SHAP. Patient 1 and 2 shows two examples of correctly predicted PNI-negative cases. Patient 3 and 4 shows two examples of correctly predicted PNI-positive cases. Pathological images were subjected to hematoxylin and eosin staining (× 100). PLR, platelet to lymphocyte ratio; SHAP, Shapley Additive explanation.

is a feasible tool for evaluating PNI status and can be used for prognostic stratification, with XGBoost machine learning being more accurate and robust.

In this multicenter study, heterogeneity was observed in the datasets from various institutions. To ensure the robustness of the subsequently established models for the different datasets, we created two additional designs. First, according to previous studies, the incidence rate of PNI varies widely, about 21.8–80%[5,23,24]. The incidence rate of PNI in the three institutions in our study was also unbalanced (38.3%, 54.8%, and 45.8%, respectively), and

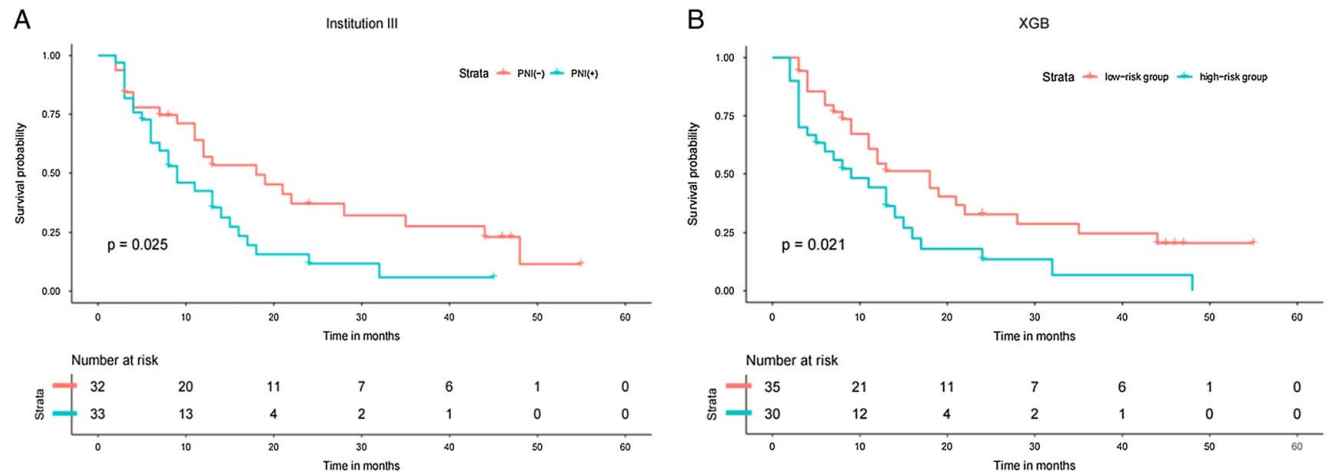

Figure 6. Kaplan–Meier curves of relapse-free survival (RFS). (A) Kaplan–Meier curves comparing RFS between perineural invasion (PNI) (+) and PNI (−) groups from institution III (hazard ratio, 1.925; 95% CI: 1.070–3.460; $P = 0.025$). (B) Kaplan–Meier curves comparing RFS between high-risk and low-risk groups from XGBoost combined model (institution III), (hazard ratio, 1.933; 95% CI: 1.093–3.418; $P = 0.021$).

we merged institutions I and II to ensure the consistency of their PNI incidence rate with the institution III (43.4%, 45.8%). Second, the CT scanning models and parameters at each institution differed. In addition, data heterogeneity was reduced through voxel resampling and grey-level discretization pre-processing. We also used the ComBat method to eliminate potential centre effects. This is a relatively novel method for image standardization[9,20,21].

Seven radiomics features, including six peritumoral features and one entire feature, successfully demonstrated the feasibility of CT radiomics features to predict PNI pathological information. Interestingly, seven radiomics features all involved the liver region surrounding the tumour. This might reflect an aggressive tendency to invade the tumour capsule and protrude into the peritumoral non-neoplastic parenchyma. The radiomics features of the peritumoral region can reflect the tumour microenvironment. Recent studies have demonstrated that neuromodulation is important in remodelling the immune microenvironment[4,25,26]. Meng *et al.*[27] also found that the PNI-positive status of ICC was associated with decreased NK cells and increased neutrophils. In addition, peritumoral radiomics features contain some important characteristics related to treatment and prognosis, confirmed in cervical[28], breast[29], and liver cancers[19,30]. Our study demonstrates the significant importance of radiomics, especially peritumoral radiomics, in predicting PNI. It may help elucidate whether PNI occurs more frequently in the tumour-periphery region and whether there is a specific association with the immune microenvironment and prognosis. These aspects warrants further investigation in our future studies.

We also evaluated preoperative clinical and radiological factors. Our results showed that PLR, tumour location, and arterial phase enhancement were independent variables associated with the PNI. PLR and NLR are commonly used peripheral blood inflammatory markers. These inflammatory factors can stimulate tumour blood vessels formation, leading to a higher invasiveness of the tumour and being associated with poor prognosis[31,32]. We speculate that PNI-positive ICC exhibits greater invasiveness, leading to a more pronounced peripheral inflammatory response. Our results recapitulate previous findings that the perihilar ICC is closely correlated with the PNI[33]; poor histological differentiation of perihilar ICC, which is more invasive, or the rich distribution of the nerve plexus around the hepatic portal may explain this[34]. Diffuse arterial hypoenhancement is another important PNI predictor. According to previous studies, tumours contain abundant fibrous stroma, leading to low enhancement in the arterial phase, which is associated with more aggressive biological behaviour and a poor prognosis[35,36], and may provide a bridge for tumour cell progression and migration, making it more likely to invade blood vessels and nerves.

Radiomics' capacity to characterize tumour size and heterogeneity may explain why the radiomics model outperformed the clinical model (DeLong's test, all $P < 0.05$). However, the radiomics model was comparable to the radiological model (DeLong's test, $P = 0.196$–0.981), and the main reason for this result may be that the CT feature-tumour location emerged as an important independent predictive factor in this study, which was not reflected by radiomics. This finding emphasizes the complementary nature of radiological features and radiomics, highlighting the importance of constructing a combined model for a comprehensive assessment of PNI status. Our results show that the combined model is better than a single model. We constructed four machine-learning models based on radscore and clinicoradiological features, and the results showed that the XGBoost model was more accurate and robust. The satisfactory results of the prospective validation cohort further demonstrated the applicability and reliability of the model. We further explored the prognostic information of the combined model, and preliminary results of this study indicate that the combined model of PNI can predict tumour recurrence stratification (HR, 1.933; 95% CI: 1.093–3.418; $P = 0.021$). Previous studies have also demonstrated the high predictive power of the XGBoost model[37,38]. Recently, interpretable machine learning has solved the "black box" phenomenon. SHAP, a highly practical machine-learning interpretation tool, can visualize each feature's overall or individual contribution and promote the clinical application of models, boosting clinicians' confidence in using predictive models[11]. The weights and effects of four independent prediction features in the combined model we have built are shown through SHAP. Case

analysis demonstrates the contributions of these four features in the case and calculates the final Shapley value, thereby obtaining the final prediction probability and achieving personalized prediction.

Our study had several limitations. Firstly, this was a retrospective and prospective study, which may have led to an information selection bias. Secondly, although this was a multicenter study, the relatively low incidence of ICC limited the sample size. Therefore, a larger sample size is required to validate the efficacy of our prediction models in future studies. Thirdly, the manual segmentation of ICC tumours was time-consuming; however, ongoing research in automated segmentation is expected to substantially reduce this workload in the future. Fourthly, the biological interpretability of radiomics remains a significant challenge, and further research is necessary to uncover the underlying connections between radiomics and genomics/proteomics. Finally, despite pathology being considered the gold standard, ICC can sometimes be indistinguishable from perihilar cholangiocarcinoma, potentially introducing bias.

Conclusion

We developed and validated a noninvasive and robust combined model incorporating CT radiomics signature and clinicoradiological features based on machine learning to identify patients' PNI status and stratify RFS. The SHAP provides a bridge for personalized prediction, which may aid clinical decision-making for the individualized treatment of ICC.

Ethics statement

This study was approved by the Institutional review board. Written informed consent was obtained from each prospectively enroled participant. For retrospective cohorts, the requirement of informed consent was waived.

Consent

Written informed consent was obtained from the patient for publication of this case report and accompanying images. A copy of the written consent is available for review by the Editor-in-Chief of this journal on request.

Sources of funding

This research was supported by the key medical talents training project of Shunde District, Foshan; the science and technology planning project of Foshan (2220001004816; 222 0001004195); Scientific Research Start Plan of Shunde Hospital, Southern Medical University (SRSP2021021); Clinical Research Start Plan of Shunde Hospital, Southern Medical University (CRSP2022005); Guangdong Medical Science and Technology Research Fund (A2023204; A2021483; A2020089); National Natural Science Foundation of China under Grant U21A 6005, Key-Area Research and Development Program of Guangdong Province (2018B030340001, 2018B030333001).

Author contribution

Z.L., C.L., B.G., and Q.H. were responsible for the overall study design. Z.L., C.L., X.C., Y.F., J.F., R.Z., X.L., Z.T., Z.C., Y.C., and X.Z. supervised the data collection. Z.L., C.L., X.C., Y.F., Z.C., J.L., and B.G. performed data analysis. Z.L., C.L., and X.C. completed manuscript drafting. Y.F., J.F., F.O., L.D., W.L., R.Z., X.L., B.G., and Q.H. were responsible for manuscript editing. All authors read, discussed, and approved the final version of the manuscript.

Conflicts of interest disclosure

The authors report no conflicts of interest.

Research registration unique identifying number (UIN)

researchregistry9714.

Guarantor

All the authors took responsibility of the final manuscript and approved it for publication.

Data availability statement

The data where our results derived from were from Shunde Hospital, Southern Medical University. The original data were not publicly available and could only be shared with the permission of the ethics committee of Shunde Hospital.

Provenance and peer review

Not commissioned, externally peer-reviewed.

References

[1] Sung H, Ferlay J, Siegel RL, *et al*. Global Cancer Statistics 2020: GLOBOCAN Estimates of Incidence and Mortality Worldwide for 36 Cancers in 185 Countries. CA Cancer J Clin 2021;71:209–49.
[2] Chen X, Du J, Huang J, *et al*. Neoadjuvant and adjuvant therapy in intrahepatic cholangiocarcinoma. J Clin Transl Hepatol 2022;10:553–63.
[3] Mazzaferro V, Gorgen A, Roayaie S, *et al*. Liver resection and transplantation for intrahepatic cholangiocarcinoma. J Hepatol 2020;72:364–77.
[4] Demir IE, Ceyhan GO, Liebl F, *et al*. Neural invasion in pancreatic cancer: the past, present and future. Cancers (Basel) 2010;2:1513–27.
[5] Wei T, Zhang XF, He J, *et al*. Prognostic impact of perineural invasion in intrahepatic cholangiocarcinoma: multicentre study. Br J Surg 2022;109:610–6.
[6] Bartsch F, Heuft LK, Baumgart J, *et al*. Influence of lymphangio (L), vascular (V), and perineural (Pn) invasion on recurrence and survival of resected intrahepatic cholangiocarcinoma. J Clin Med 2021;10:2426.
[7] Tang H, Lu W, Li B, *et al*. Influence of surgical margins on overall survival after resection of intrahepatic cholangiocarcinoma: a meta-analysis. Medicine (Baltimore) 2016;95:e4621.
[8] Zhang XF, Bagante F, Chakedis J, *et al*. Perioperative and long-term outcome for intrahepatic cholangiocarcinoma: impact of major versus minor hepatectomy. J Gastrointest Surg 2017;21:1841–50.
[9] Chen X, He L, Li Q, *et al*. Non-invasive prediction of microsatellite instability in colorectal cancer by a genetic algorithm-enhanced artificial neural network-based CT radiomics signature. Eur Radiol 2023;33:11–22.
[10] Wang K, Tian J, Zheng C, *et al*. Interpretable prediction of 3-year all-cause mortality in patients with heart failure caused by coronary heart disease based on machine learning and SHAP. Comput Biol Med 2021;137:104813.

[11] Ma J, Bo Z, Zhao Z, *et al*. Machine learning to predict the response to lenvatinib combined with transarterial chemoembolization for unresectable hepatocellular carcinoma. Cancers (Basel) 2023;15:625.
[12] McShane LM, Altman DG, Sauerbrei W, *et al*. REporting recommendations for tumour MARKer prognostic studies (REMARK). Br J Cancer 2005;93:387–91.
[13] Ebata T, Kosuge T, Hirano S, *et al*. Proposal to modify the International Union Against Cancer staging system for perihilar cholangiocarcinomas. Br J Surg 2014;101:79–88.
[14] Dissaux G, Visvikis D, Da-Ano R, *et al*. Pretreatment (18)F-FDG PET/CT radiomics predict local recurrence in patients treated with stereotactic body radiotherapy for early-stage non-small cell lung cancer: a multicentric study. J Nucl Med 2020;61:814–20.
[15] Ligero M, Jordi-Ollero O, Bernatowicz K, *et al*. Minimizing acquisition-related radiomics variability by image resampling and batch effect correction to allow for large-scale data analysis. Eur Radiol 2021;31:1460–70.
[16] van Griethuysen JJM, Fedorov A, Parmar C, *et al*. Computational radiomics system to decode the radiographic phenotype. Cancer Res 2017;77:e104–7.
[17] Ji GW, Zhu FP, Xu Q, *et al*. Radiomic features at contrast-enhanced CT predict recurrence in early stage hepatocellular carcinoma: a multi-institutional study. Radiology 2020;294:568–79.
[18] Chen S, Feng S, Wei J, *et al*. Pretreatment prediction of immunoscore in hepatocellular cancer: a radiomics-based clinical model based on Gd-EOB-DTPA-enhanced MRI imaging. Eur Radiol 2019;29:4177–87.
[19] Chong H, Gong Y, Pan X, *et al*. Peritumoral dilation radiomics of gadoxetate disodium-enhanced MRI excellently predicts early recurrence of hepatocellular carcinoma without macrovascular invasion after hepatectomy. J Hepatocell Carcinoma 2021;8:545–63.
[20] Orlhac F, Lecler A, Savatovski J, *et al*. How can we combat multicenter variability in MR radiomics? Validation of a correction procedure. Eur Radiol 2021;31:2272–80.
[21] Da-Ano R, Masson I, Lucia F, *et al*. Performance comparison of modified ComBat for harmonization of radiomic features for multicenter studies. Sci Rep 2020;10:10248.
[22] Cooper ME, Risk B, Corey A, *et al*. Statistical learning of blunt cerebrovascular injury risk factors using the elastic net. Emerg Radiol 2021;28:929–37.
[23] Shirai K, Ebata T, Oda K, *et al*. Perineural invasion is a prognostic factor in intrahepatic cholangiocarcinoma. World J Surg 2008;32:2395–402.
[24] Zhang Z, Zhou Y, Hu K, *et al*. Perineural invasion as a prognostic factor for intrahepatic cholangiocarcinoma after curative resection and a potential indication for postoperative chemotherapy: a retrospective cohort study. BMC Cancer 2020;20:270.
[25] Yang MW, Tao LY, Jiang YS, *et al*. Perineural invasion reprograms the immune microenvironment through cholinergic signaling in pancreatic ductal adenocarcinoma. Cancer Res 2020;80:1991–2003.
[26] Tan X, Sivakumar S, Bednarsch J, *et al*. Nerve fibers in the tumor microenvironment in neurotropic cancer-pancreatic cancer and cholangiocarcinoma. Oncogene 2021;40:899–908.
[27] Meng XL, Lu JC, Zeng HY, *et al*. The clinical implications and molecular features of intrahepatic cholangiocarcinoma with perineural invasion. Hepatol Int 2023;17:63–76.
[28] Sun C, Tian X, Liu Z, *et al*. Radiomic analysis for pretreatment prediction of response to neoadjuvant chemotherapy in locally advanced cervical cancer: a multicentre study. EBioMedicine 2019;46:160–9.
[29] Braman N, Prasanna P, Whitney J, *et al*. Association of peritumoral radiomics with tumor biology and pathologic response to preoperative targeted therapy for HER2 (ERBB2)-positive breast cancer. JAMA Netw Open 2019;2:e192561.
[30] Kim S, Shin J, Kim DY, *et al*. Radiomics on gadoxetic acid-enhanced magnetic resonance imaging for prediction of postoperative early and late recurrence of single hepatocellular carcinoma. Clin Cancer Res 2019;25:3847–55.
[31] Chen Q, Dai Z, Yin D, *et al*. Negative impact of preoperative platelet-lymphocyte ratio on outcome after hepatic resection for intrahepatic cholangiocarcinoma. Medicine (Baltimore) 2015;94:e574.
[32] Huh G, Ryu JK, Chun JW, *et al*. High platelet-to-lymphocyte ratio is associated with poor prognosis in patients with unresectable intrahepatic cholangiocarcinoma receiving gemcitabine plus cisplatin. BMC Cancer 2020;20:907.
[33] Aishima S, Kuroda Y, Nishihara Y, *et al*. Proposal of progression model for intrahepatic cholangiocarcinoma: clinicopathologic differences between hilar type and peripheral type. Am J Surg Pathol 2007;31:1059–67.
[34] Zhang XF, Bagante F, Chen Q, *et al*. Perioperative and long-term outcome of intrahepatic cholangiocarcinoma involving the hepatic hilus after curative-intent resection: comparison with peripheral intrahepatic cholangiocarcinoma and hilar cholangiocarcinoma. Surgery 2018;163:1114–20.
[35] Min JH, Kim YK, Choi SY, *et al*. Intrahepatic mass-forming cholangiocarcinoma: arterial enhancement patterns at MRI and prognosis. Radiology 2019;290:691–9.
[36] Fujita N, Asayama Y, Nishie A, *et al*. Mass-forming intrahepatic cholangiocarcinoma: Enhancement patterns in the arterial phase of dynamic hepatic CT - Correlation with clinicopathological findings. Eur Radiol 2017;27:498–506.
[37] Mao B, Zhang L, Ning P, *et al*. Preoperative prediction for pathological grade of hepatocellular carcinoma via machine learning-based radiomics. Eur Radiol 2020;30:6924–32.
[38] Xu Q, Lu X. Development and validation of an XGBoost model to predict 5-year survival in elderly patients with intrahepatic cholangiocarcinoma after surgery: a SEER-based study. J Gastrointest Oncol 2022;13:3290–9.